Lawrence Berkeley National Laboratory
LBL Publications

Title

The Effect of Fault Geometry and Minimum Shear Wavespeed on 3D Ground-Motion Simulations for an Mw 6.5 Hayward Fault Scenario Earthquake, San Francisco Bay Area, Northern CaliforniaThe Effect of Fault Geometry and Minimum Shear Wavespeed on 3D Ground...

Permalink

Journal

ISSN

Authors

Rodgers, Arthur J
Pitarka, Arben
McCallen, David B

Publication Date

DOI

Peer reviewed

The Effect of Fault Geometry and Minimum Shear Wavespeed on 3D Ground-Motion Simulations for an M_w 6.5 Hayward Fault Scenario Earthquake, San Francisco Bay Area, Northern California

by Arthur J. Rodgers,[*] Arben Pitarka, and David B. McCallen[†]

Abstract We investigated the effects of fault geometry and assumed minimum shear wavespeed ($V_{S\min}$) on 3D ground-motion simulations (0–2.5 Hz) in general, using a moment magnitude (M_w) 6.5 earthquake on the Hayward fault (HF). Simulations of large earthquakes on the northeast-dipping HF using the U.S. Geological Survey (USGS) 3D seismic model have shown intensity asymmetry with stronger shaking for the Great Valley Sequence east of the HF (hanging wall) relative to the Franciscan Complex to the west (footwall). We performed simulations with three fault geometries in both plane-layered (1D) and 3D models. Results show that the nonvertical fault geometries result in larger motions on the hanging wall relative to the vertical fault for the same Earth model with up to 50% amplifications in single-component peak ground velocity (PGV) within 10 km of the rupture. Near-fault motions on the footwall are reduced for the nonvertical faults, but less than they are increased on the hanging wall. Simulations assuming $V_{S\min}$ values of 500 and 250 m/s reveal that PGVs are on average 25% higher west of the HF when using the lower $V_{S\min}$, with some locations amplified by a factor of 3. Increasing frequency content from 2.5 to 5 Hz increases PGV values. Spectral ratios of these two $V_{S\min}$ cases show average amplifications of 2–4 (0.5–1.5 Hz) for the lower $V_{S\min}$ west of the fault. Large differences (up to 2×) in PGV across the HF from previous studies persist even for the case with a vertical fault or $V_{S\min}$ of 250 m/s. We conclude that assuming a $V_{S\min}$ of 500 m/s underestimates intensities west of the HF for frequencies above 0.5 Hz, and that low upper crustal (depth < 10 km) shear wavespeeds defined in the 3D model contribute most to higher intensities east of the HF.

Introduction

Numerical simulation of earthquake ground motions in 3D Earth models is of particular interest for seismic hazard and engineering applications for near-fault sites where damage to structures tends to be most prevalent. Near-fault motions can be highly variable and recorded data are sparse (e.g., Bakun *et al.*, 2005; Bozorgnia *et al.*, 2014). Simulations offer an attractive alternative to reliance on limited empirical data. These specify 3D Earth structure and the earthquake rupture, and then solve for the time evolution of seismic-wave propagation throughout a limited computational domain spanning the rupture and near-fault locations of interest. Kinematic source models informed by scaling relations and dynamic rupture modeling provide realistic excitation of seismic waves in arbitrary fault geometries. Simulation of wave propagation through 3D Earth models includes important path and site effects such as amplification by sedimentary basins, mode conversions at structural interfaces, and focusing and scattering by material heterogeneity. As numerical simulations become more realistic through advances in numerical algorithms, Earth model improvements and computational methods as well as the inexorable progression of high-performance computing (HPC), it is important to understand how various assumptions and limitations impact the results. In fact, numerical simulations enable carefully controlled, numerical experiments that cannot be reproduced in nature to test how variations in a single or small set of parameters impact the ground-motion response.

---

*Also at Earth and Environmental Sciences Area, Lawrence Berkeley National Laboratory, 1 Cyclotron Road, MS74R316C, Berkeley, California 94720 U.S.A.; and Berkeley Seismological Laboratory, University of California, 307 McCone Hall #4760, Berkeley, California 94720-4760 U.S.A.

†Also at Department of Civil and Environmental Engineering, University of Nevada, 1644 North Virginia Street, Reno, Nevada 89577-0258 U.S.A.

Fully deterministic earthquake ground-motion simulations in 3D Earth models require fine spatial discretization to resolve high frequencies of engineering interest, above 1 Hz and as high as 5–10 Hz. The resolved highest frequency depends on the grid spacing and the lowest wavespeed, typically the near-surface soft sediment shear wavespeeds (V_S). Several numerical methods have been used to compute earthquake ground motions in 3D Earth models including finite difference (e.g., Olsen *et al.*, 1995; Graves, 1996; Pitarka, 1999; Moczo *et al.*, 2014), finite element (e.g., Aagaard *et al.*, 2001; Taborda and Bielak, 2011), and spectral element (e.g., Komatitsch and Tromp, 1999; Chaljub *et al.*, 2007; Peter *et al.*, 2011). Regardless of the numerical method or code, these simulations require HPC to resolve frequencies of engineering interest and span the spatial domains for large earthquakes (moment magnitude M_w greater than about 6.0), including rupture lengths of 20 km or more.

Time-domain numerical methods such as finite difference, finite element, and spectral element need sufficiently fine spatial discretization to resolve high frequency, short-wavelength waves. This requires a certain number of grid points-per-minimum wavelength (PPW), such that the shortest wavelength λ_{min} corresponding to the highest frequency f_{max}, follows $\lambda_{min} = h_{min} \times \text{PPW}$, in which h_{min} is the minimum grid spacing near the surface, say between finite-different grid points, finite-element nodes, or Gauss–Lobatto–Legendre points. The highest resolved frequency f_{max} depends on the minimum wavespeed V_{min} (usually the shear wavespeed at the surface) according to $f_{max} = V_{min}/\lambda_{min} = V_{min}/(h_{min} \times \text{PPW})$.

Near-surface shear wavespeeds can have a profound impact on earthquake ground motion and are correlated with the depositional environment and deeper crustal structure. Geotechnical characterization of the near-surface soil and rock properties is important for site response and seismic hazard assessment (Joyner and Boore, 1988; Kramer, 1996; Boore, 2004). The slowness-averaged shear wavespeed of the upper 30 m (~100 ft), V_{S30}, is now commonly used in site characterization and ground-motion prediction equations and is related to ground-motion intensities. Incorporation of low-velocity geotechnical properties into large-scale simulations remains a computational challenge (e.g., Flinchum *et al.*, 2014; Taborda *et al.*, 2016).

It is common practice in 3D ground-motion simulations to use an artificially high-minimum shear wavespeed. There are two points that inform this choice. First, it is computationally expensive to represent fine-scale (a few to tens of meters) near-surface material properties for large domains (hundreds of kilometers) while obtaining the desired high-frequency content within the constraints of available computational resources. Second, weak, low-shear-wavespeed material in the near surface, such as unconsolidated soils, can behave nonlinearly in response to strong shaking (Hartzell *et al.*, 2004; Bonilla *et al.*, 2005). Nonlinear geomechanics of the near surface can be handled within the large-scale simulation (e.g., Roten *et al.*, 2014, 2017; Fu *et al.*, 2017) or in

separate postprocessing to modify motions according to empirical scaling laws (e.g., Liu *et al.*, 2006; Pitarka *et al.*, 2013). Importantly, nonlinear material response tends to modify amplitudes and shift site-response resonances to lower frequencies. A related challenge to the topic of $V_{S\,min}$ is that our knowledge of detailed geotechnical properties across large regions is limited, but efforts to improve this are ongoing (e.g., Wills and Clahan, 2006; Flinchum *et al.*, 2014; Yong *et al.*, 2016; Pancha *et al.*, 2017). Creating scalable models for near-surface soil properties and their correlation structure will improve seismic hazard assessments (Shi and Asimaki, 2018).

Several earthquake ground-motion studies in the San Francisco Bay area (SFBA) of northern California utilized a 3D geologic and seismic model developed by the U.S. Geological Survey (USGS) (Brocher, 2005a; Aagaard *et al.*, 2008; U.S. Geological Survey [USGS], 2019; hereafter, referred to simply as the USGS 3D model). This model is based on constraints from geology and geophysics. The Hayward fault (HF) forms a structural boundary between geologically and lithologically distinct rocks with the metamorphic assemblage Franciscan Complex to the west and the sedimentary Great Valley Sequence to the east (Ponce *et al.*, 2004; Graymer *et al.*, 2005). The USGS 3D model includes V_S as low as 80 m/s for the sediments underlying San Francisco Bay (discussed subsequently). Harmsen *et al.* (2008) simulated strong motions to 1 Hz around the Santa Clara Valley for southern HF and Calaveras fault ruptures and set $V_{S\,min}$ to 330 m/s. A large suite of Hayward and Rodgers Creek fault 3D simulations was performed with similar resolution by five groups and reported in Aagaard *et al.* (2010) using a $V_{S\,min}$ of 500–700 m/s. In three recent simulation studies of a moment magnitude M_w 7.0 HF scenario earthquake, motions were resolved to 2.5, 4.2, and 5.0 Hz using $V_{S\,min}$ set to 500 m/s (Johansen *et al.*, 2017; Rodgers, Petersson, *et al.*, 2018; Rodgers, Pitarka, *et al.*, 2018; Rodgers *et al.*, 2019).

Ground motions computed to date using the USGS 3D model for large ruptures on the HF generally show higher amplitudes east of the fault compared to the west. Figure 1 shows maps of the peak ground velocity (PGV) from two recent simulation studies for different M_w 7.0 HF ruptures (Rodgers, Pitarka, *et al.*, 2018; Rodgers *et al.*, 2019). These resolved motions to 4.2 and 5 Hz, respectively, while assuming a $V_{S\,min}$ of 500 m/s. HF geometry is indicated by locations of the upper and lower limit of the rupture surface. These simulations used different rupture dimensions with Rodgers, Pitarka *et al.* (2018) using a shorter wider fault (50×20 km) spanning the northern and central HF, and Rodgers *et al.* (2019) used a longer narrower fault (77×14 km). Both cases projected the slip onto the geometry of the HF as specified by the USGS 3D model. The pattern of PGV for both cases shows higher amplitudes east of the fault relative to lower amplitudes to the west in the northern segment near Richmond, Berkeley, and Orinda. In the central and southern segments, the amplitudes are large on both sides of
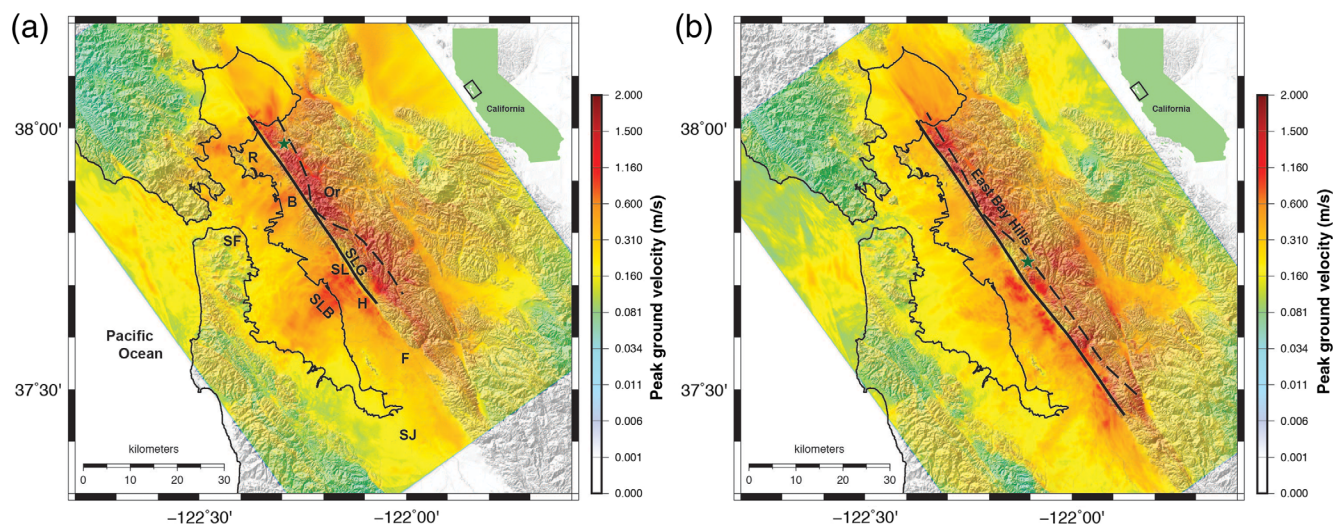
Figure 1. Maps of peak ground velocities (PGVs, scale bar) for two simulations of M_w 7.0 Hayward fault (HF) earthquakes with different hypocenters (stars), slip distributions, and rupture lengths. (a) 50 km long (Rodgers, Petersson, *et al.*, 2018) and (b) 77 km long (Rodgers *et al.*, 2019). Each panel shows the participating HF segment (top and bottom of rupture as solid and dashed lines). The East Bay Hills are labeled in (b). Features identified in (a) are: B, Berkeley; F, Fremont; H, Hayward; R, Richmond; Or, Orinda; SF, San Francisco; SJ, San Jose; SL, San Leandro; SLB, San Leandro basin; SLG, San Leandro Gabbro. The inset map of California shows each domain and provides orientation on a larger scale. The color version of this figure is available only in the electronic edition.

the fault outside of the San Leandro Gabbro near the San Leandro basin and cities of Hayward and Fremont. The San Leandro Gabbro is a high-wavespeed ophiolite body along the HF (Ponce *et al.*, 2003). The PGV values in Figure 1 show a pattern of high amplitudes around this feature and low values within it. The San Leandro basin (Brocher, 2005b; Sneed *et al.*, 2015) is a sedimentary structure of moderate depth (1.5 km) spanning the San Francisco Bay shoreline for about 20 km northwest–southeast. This feature shows high PGV values, particularly for the case in Figure 1a.

A complicating factor in the computed PGV maps is the geometry of the HF (Fig. 1). The HF is a major strike-slip fault, but its dip is near-vertical only in the vicinity of north Oakland and Berkeley. It dips to the northeast in the central and southern segments near San Leandro, Hayward, and Fremont and in the northernmost segment near Richmond (Ponce *et al.*, 2004; Graymer *et al.*, 2005, their fig. 3H). In the central segment of the HF near San Leandro, the fault is listric. In the long-dipping segments, the fault underlies the Great Valley Sequence on the hanging wall. Usually, in reverse thrust mechanism earthquakes (e.g., 1994 M_w 6.7 Northridge, 1999 M_w 7.6 Chi-Chi) the hanging wall exhibits higher motions than the footwall (Abrahamson and Somerville, 1996). This phenomenon has been confirmed with numerical simulations (e.g., Aagaard *et al.*, 2004; Donahue and Abrahamson, 2014). Recently, Passone and Mai (2017) used simulations to show how listric normal faults result in more asymmetry in ground-motion amplitudes across the fault.

Obviously, seismic wavespeed structure plays a major role in controlling the pattern of PGV in the numerical simulations shown in Figure 1. The high PGV values in the East Bay Hills, east of the HF are coincident with the sedimentary

Great Valley Sequence. Low-wavespeed sedimentary rocks ($V_S \leq 2000$ m/s and compressional wavespeed $V_P \leq 4000$ m/s) of the Great Valley Sequence are present to depths to 2 km or more. Evidence of this is seen in the Trollman 1 and Bethlehem 1 sonic log data (V_P) from Brocher (2005b, his fig. 12A) and scaling relations in Brocher (2008).

The Franciscan Complex underlies the cities of Berkeley, Oakland, San Leandro, Hayward, Fremont, the East Bay shoreline, and the San Francisco Bay west of the HF (e.g., Graymer *et al.*, 2005). In the USGS 3D model, this geologic unit is characterized by thin (≤ 75 m) sedimentary surface deposits outside of the San Leandro basin with low wavespeeds ($V_S < 500$ m/s) underlain by higher wavespeed rock ($V_S > 500$ m/s). Geotechnical studies along the East Bay shoreline (e.g., Holzer, Bennett, *et al.*, 2005; Holzer, Padovani, *et al.*, 2005; Yong *et al.*, 2016) report V_{S30} values of 100–400 m/s.

The pattern of motions seen in previous scenario earthquake ground-motion simulations (such as those in Fig. 1) has been discussed in Aagaard *et al.* (2010), Rodgers, Petersson, *et al.* (2018), Rodgers, Pitarka, *et al.* (2018), and Rodgers *et al.* (2019). However, to date, ground-motion simulations have not honored the low near-surface shear wavespeeds in the Franciscan Complex west of the HF. Thus, it remains an important open question as to whether the observed asymmetry in PGV maps across the HF will persist in numerical simulations using a reduced $V_{S\,min}$ that more faithfully honors the USGS 3D model. Furthermore, the accuracy of the USGS 3D model deserves investigation with waveform data from small-to-moderate earthquakes, which is beyond the scope of this study but the subject of ongoing investigations.

In light of previous 3D HF ground-motion simulation studies and the entangled combination of fault geometry and geologic/seismic structure, we consider the following questions in this article:

- How much does the dipping HF geometry contribute to weaker motions on the footwall and stronger motions on the hanging wall?
- What is being missed in ground-motion simulations using a $V_{S \min}$ value of 500 m/s, which is higher than the values indicated for the western side of the HF in the USGS 3D model?

These questions are interrelated. Weaker motions in the urbanized East Bay cities and shoreline could result from footwall effects or from the assumed higher $V_{S \min}$ of 500 m/s for these areas composed of Franciscan Complex west of the HF. Stronger motions in the Great Valley Sequence east of the HF could result from hanging-wall effects as well as the low-wavespeed material of these sedimentary rocks.

In this study, we simulated ground motions from an M_w 6.5 earthquake on the HF. A smaller magnitude was chosen to reduce the domain size compared to M_w 7.0 ruptures and allow calculation of higher resolution with lower $V_{S \min}$. Figure 2 shows the study area and computational domain. The domain includes the cities of Oakland, Berkeley, San Leandro, Hayward, Castro Valley, Fremont, Orinda, and Moraga located along the HF, as well as San Francisco, Walnut Creek, San Ramon, Pleasanton, and Livermore. We quantify the impact of fault geometry on asymmetries in the ground-motion intensities across the fault by computing the relative response for three fault geometries with all other source properties equal. We also investigated the impact of the assumed minimum shear wavespeed $V_{S \min}$ on simulated ground motions to develop insight into what is missed by assuming higher values than those specified in the USGS 3D model, and that actually exist in independent field measurements. Although we report on specific details for the HF, the subjects of fault geometry for dipping strike-slip faults and assumed $V_{S \min}$ are relevant to ground-motion simulations in other areas.

In the following section, we describe the USGS 3D Earth within the study area, the computational details, and source models. This is followed by a presentation of the results in terms of the impact on ground motions of the fault geometry and the assumed $V_{S \min}$ values. Finally, we discuss the implications of the results and make recommendations for future advancements of fully deterministic scenario earthquake modeling.

The USGS 3D SFBA Model

The USGS 3D model provides the most detailed representation of subsurface material properties for the SFBA (Brocher, 2005a; Graymer et al., 2005; USGS, 2019). The geometry of the HF in the model was determined from
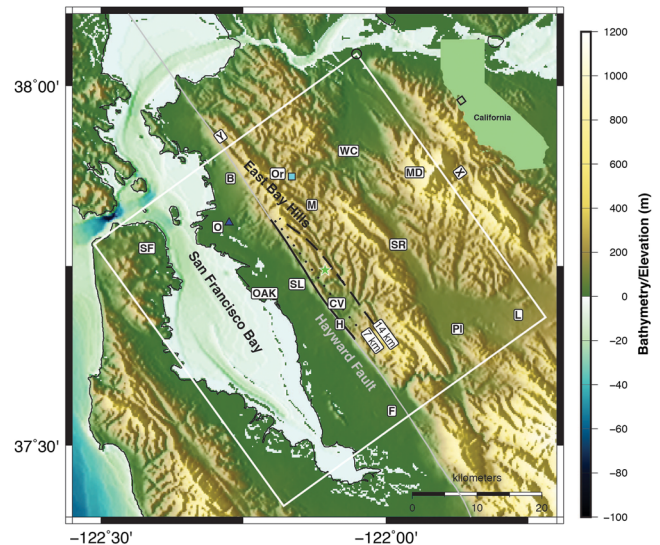

Figure 2. Map of the study area around the HF, San Francisco Bay Area (SFBA), northern California with bathymetry and topography (scale). The HF is indicated by the gray line with the rupture segment considered here indicated by the surface projections of the top and depths of 7 and 14 km (thick, dotted, and dashed black lines, respectively). The hypocenter is indicated by the star. The computational domain (white box), origin (circle), and Cartesian directions (X and Y used in later figures) are shown. The locations of shear-wavespeed profiles shown in Figure 4 are indicated by the triangle and square (Oakland and Orinda, respectively). City and place names not shown in Figure 1 are indicated: CV, Castro Valley; L, Livermore; M, Moraga; MD, Mount Diablo; O, Oakland; OAK, Oakland Airport; Pl, Pleasanton; SF, San Francisco; SR, San Ramon; WC, Walnut Creek. The color version of this figure is available only in the electronic edition.

geology and geophysics (Ponce et al., 2003, 2004; Graymer et al., 2005) including precise earthquake locations (Waldhauser and Ellsworth, 2002; Hardebeck et al., 2007; Waldhauser and Schaff, 2008). The fault surface is specified in a self-consistent manner so that the HF represents the surface separating different geologic and lithologic units. The dip and 3D fault geometry are indicated with depth levels in Figures 1 and 2. For most of its extent, the HF dips to the northeast with a minimum (shallowest) dip angle of about 75° in the central segment that we consider here (near south Oakland, San Leandro, and Castro Valley, Fig. 2).

Figure 3 shows various features of the shear-wavespeed properties of the USGS 3D model in map view for the domain considered here. The model was interpolated from its native resolution to a finer grid spacing (12.5 m) to resolve frequencies above 1 Hz. The surface V_S following local topography and bathymetry shown in Figure 3a reveals low-shear wavespeeds (≤ 500 m/s) associated with near-surface sedimentary geology along San Francisco Bay shore west of the HF. The very high V_S body along the HF is noted. This is the San Leandro Gabbro (also called the Coast Range Ophiolite) and its effect in reducing ground-motion amplitudes is seen in Figure 1 and was discussed in Rodgers, Pitarka, et al. (2018) and Rodgers et al. (2019). We also show
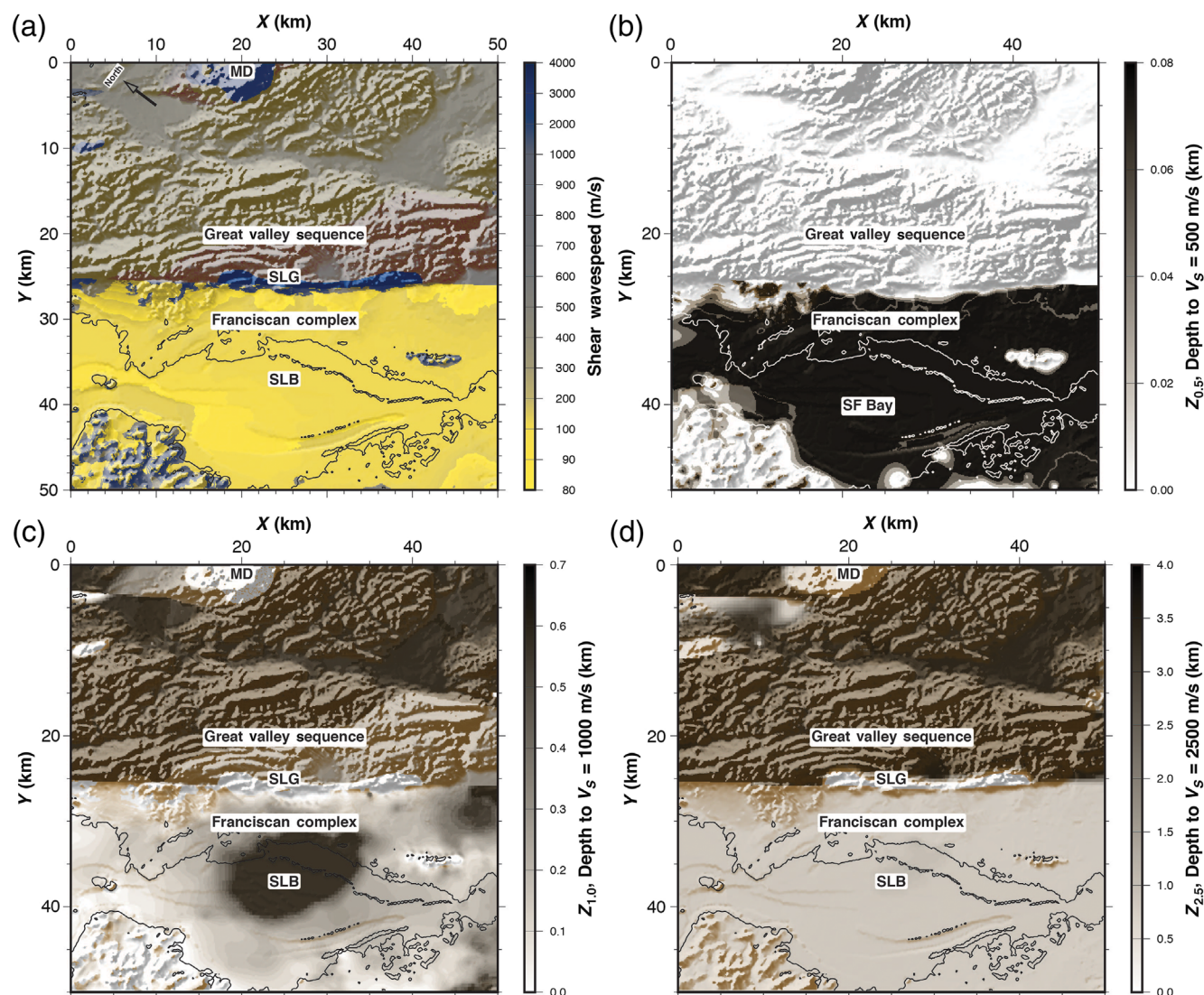
Figure 3. Shear wavespeed V_S properties of the computational domain (USGS, 2019). (a) Surface V_S and (b,c,d) the depths to the V_S values of 500, 1000, and 2500 m/s, respectively. The color version of this figure is available only in the electronic edition.

the depths to the 500, 1000, and 2500 m/s shear wavespeeds ($Z_{0.5}$, $Z_{1.0}$ and $Z_{2.5}$, respectively) in Figure 3b,c,d. Some ground-motion models use such site-specific parameters as proxies for basin amplification effects on ground-motion intensities (e.g., Abrahamson *et al.*, 2014; Campbell and Bozorgnia, 2014; Chiou and Youngs, 2014).

Figure 3 reveals the complex 3D seismic structure of the SFBA. Near the surface, the Franciscan Complex rocks west side of the HF have lower V_S than the Great Valley Sequence (east of the HF). However, the relationship reverses at depth with low V_S values in the Great Valley Sequence on the east side and higher values in the Franciscan Complex west of the fault. The San Leandro basin is clearly seen in the $Z_{1.0}$ (Fig. 3c). The $Z_{0.5}$ map (Fig. 3b) shows large areas west of the HF in which the assumption of a $V_{S\,\mathrm{min}}$ of 500 m/s does not honor the USGS 3D model, but these areas have at most only 75 m of lower V_S material.

To illustrate the differences in seismic properties of near surface and the deeper crust across the HF, we show vertical profiles of shear wavespeeds at two locations (Oakland and Orinda, west and east of the HF, respectively, as indicated in Fig. 2) and average 1D models in Figure 4. Figure 4a shows the near-surface V_S (0–300 m). Here, the Orinda profile shows V_S is about 500 m/s at the surface and increases slowly with depth. However, in Oakland V_S is 130 m/s at the surface and increases rapidly with depth reaching 500 m/s at 75 m depth. On the upper crustal scale (Fig. 4b), the two V_S profiles are dramatically different, with the eastern side of the HF in Orinda having much lower values than the western side in Oakland. The differences between the eastern and western sides of the HF persist to about 10 km (Fig. 4c). The seismic wavespeeds on opposite sides of the HF were seen in figure 15 of Brocher (2005a) for the Franciscan Complex rocks and Great Valley Sequence. We also show plane-layered (1D)
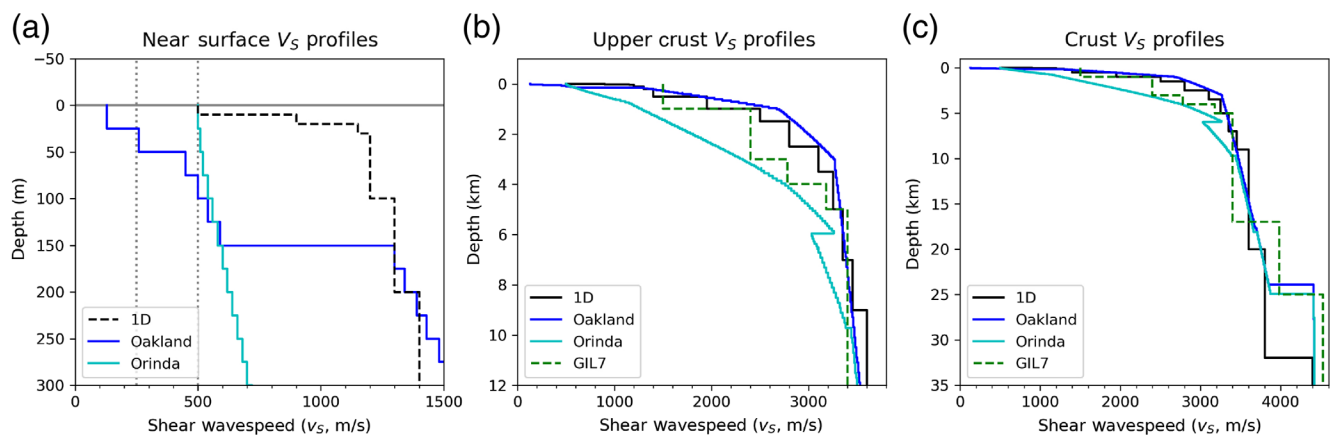
Figure 4. Shear-wavespeed profiles for the depth below the surface for our 1D model (based on Kamai *et al.*, 2014, see The USGS 3D SFBA Model section) and two locations in the U.S. Geological Survey (USGS) 3D model: Oakland and Orinda (locations indicated in Fig. 2). (a) Near surface, (b) upper crustal, and (c) full crustal scale depths are shown with different depth scales. For the near-surface profiles in (a), we show the 250 and 500 m/s $V_{S\min}$ values as dotted gray lines. The GIL7 model (Dreger and Romanowicz, 1994) is shown in (b) and (c). The color version of this figure is available only in the electronic edition.

models in Figure 4. Kamai *et al.* (2014; hereafter, KAG) reported an average 1D model for the SFBA based on sites that recorded the 1989 Loma Prieta earthquake. We used a variant of the KAG model with minimum layer thickness of 10 m and $V_{S\min}$ of 500 m/s, which is labeled 1D in Figure 4. For reference, we show the GIL7 model (Dreger and Romanowicz, 1994), which is used by the University of California Berkeley Seismology Laboratory for routine complete waveform modeling of moment tensors. The V_S profile in Oakland is very similar to the 1D model.

Computational Details

We simulated 60 s of seismogram duration for a volume spanning 50×50 km laterally to a depth of 35 km for an M_w 6.5 earthquake rupture. All numerical ground-motion simulations were performed with SW4 (seismic waves, fourth order), a finite-difference code based on the summation-by-parts principle for seismic-wave simulations on parallel computers (Petersson and Sjogreen, 2012, 2014, 2015, 2018; Sjogreen and Petersson, 2012). SW4 solves the displacement formulation with a node-centered fourth-order finite-difference method. Surface topography is represented by a curvilinear mesh that stretches the mesh vertically to conform to user-specified topography. The curvilinear mesh transitions to a Cartesian mesh, which can be coarsened to increase the grid spacing as wavespeeds increase with depth. We considered wave excitation and propagation in both the average 1D and USGS 3D Earth models. The calculations with the 1D model had a flat free surface. The 3D model included surface topography, which extends from Mount Diablo (1132 m) to the San Francisco Bay ship channel (−30 m) for this domain (Fig. 2). The highest resolved frequency used for comparing simulated ground motions presented in this study is 2.5 Hz, with one exception in which we computed motions to 5.0 Hz. Parameters used for various cases considered below are compiled in Table 1, including the $V_{S\min}$, $h_{\min}$, and $f_{\max}$. These

cases are discussed in detail below. All cases used 8 PPW and had two mesh refinements. The large domain and fine resolution of these simulations required on the order 1–7 billion grid points and consequently simulations were performed on high-performance computers.

We generated a finite-rupture model for a hypothetical M_w 6.5 earthquake on the HF using the methods of Graves and Pitarka (2010, 2015, 2016). This method generates a slip distribution based on a von Karman correlation function following properties of empirical finite-fault models (e.g., Somerville *et al.*, 1999; Mai and Beroza, 2002). Figure 5 shows the distributions of slip, duration, and rake on the fault surface. The rupture front propagates more rapidly through large slip areas and more slowly through low slip areas. The rake varies randomly with a similar spatial correlation structure as the slip. The rupture area is computed following KAG with length 22.6 km and width 14 km spanning seismogenic depths (e.g., Waldhauser and Ellsworth, 2002). The

Table 1
Simulations Performed

Case	Fault Geometry*	Earth Model	$V_{S\min}$ (m/s)	$h_{\min}$ (m)	$f_{\max}$ (Hz)	N_{points}
1	vf	1DFLAT	500	25	2.5	7.815×10^8
2	pf	1DFLAT	500	25	2.5	7.815×10^8
3	cf	1DFLAT	500	25	2.5	7.815×10^8
4	vf	3DTOPO	500	25	2.5	8.696×10^8
5	pf	3DTOPO	500	25	2.5	8.696×10^8
6	cf	3DTOPO	500	25	2.5	8.696×10^8
7	cf	3DTOPO	250	12.5	2.5	6.7163×10^9
8	cf	3DTOPO	500	12.5	2.5	6.7163×10^9
9	cf	3DTOPO	500	12.5	5.0	6.7163×10^9

$f_{\max}$, maximum frequency resolved with 8 points per wavelength (PPW) or applied source prefilter; $h_{\min}$, minimum grid spacing; N_{points}, total number of grid points in simulation; $V_{S\min}$, minimum shear wavespeed.

*vf, vertical fault, dip = 90°; pf, planar fault, dip = 75°; cf, curved fault, following U.S. Geological Survey (USGS) 3D model.
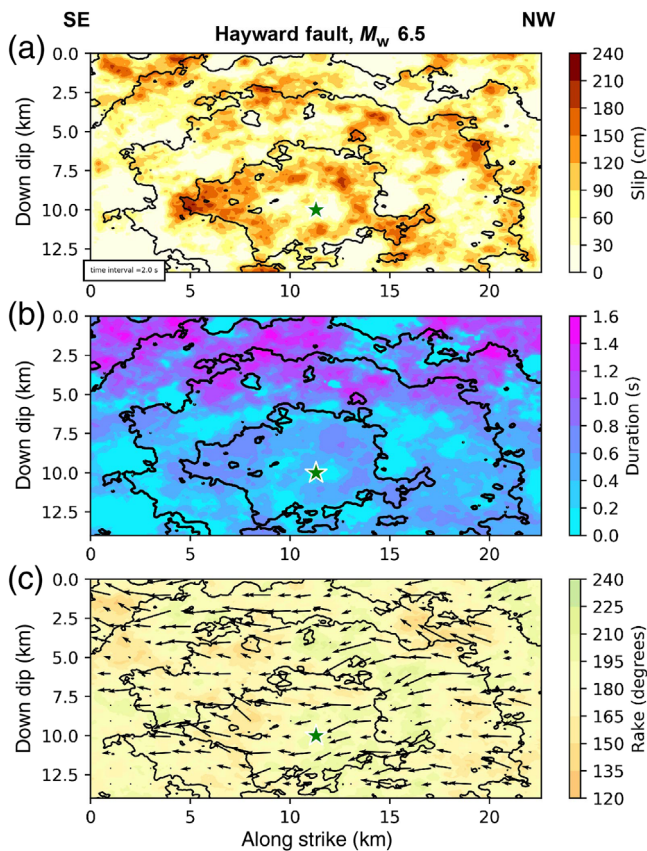
Figure 5. Rupture model showing the (a) slip, (b) duration, and (c) rake. In each panel, the hypocenter (star) and contours of rupture time (2 s) are shown. The coordinates are for the planar fault surface and the southeast (SE, left) and northwest (NW, right) corners are labeled. The color version of this figure is available only in the electronic edition.

rupture was partitioned into 100 m subfaults. The top of the rupture was arbitrarily located at 1 km below sea level, and the rupture model is projected onto the northeast-dipping HF geometry as specified by the USGS 3D model. The hypocenter at 11 km depth (below sea level) is located near the San Leandro salient, where the HF reveals complex focal mechanisms suggesting stress concentration in which events nucleate or terminate (Waldhauser and Ellsworth, 2002; Hardebeck et al., 2007; Waldhauser and Schaff, 2008). Only one rupture model was considered in this study and results with other ruptures may be different. To address this, we used differential intensity measurements that should isolate the effects of fault geometry or near-surface shear-wavespeed structure.

Impact of Fault Geometry on Ground Motions

The impact of fault geometry on ground motions was considered with three fault geometries: a vertical fault with a dip angle of 90°, a planar fault with a dip angle of 75°, and a curved fault following the USGS 3D model. Motions for three fault geometries were considered in the 1D and 3D Earth models. The 1D model allowed us to simplify the response and look at the symmetry across the fault unbiased

by complex path and site effects. This first set of simulations (cases 1–6, Table 1) had a maximum frequency of 2.5 Hz using a minimum grid spacing h_{min} of 25 m. Both the 1D and 3D models assumed a minimum shear wavespeed $V_{S\,min}$ of 500 m/s.

Figure 6 shows single-component PGV maps for the three fault geometries, obtained with the 1D and 3D models at the resolution of the calculations (25 m). These maps (like those shown in Fig. 1) display the maximum horizontal ground motion on either the x- or y component, not the polarization-independent measurement used in the RotD50 spectral accelerations (Boore et al., 2006; Boore, 2010). The vertical fault (case 1, Fig. 6a) shows a mostly symmetric pattern of intensities across the fault. Variations from pure uniform rake on the fault (i.e., strike slip with rake = 180° everywhere) are part of the Graves and Pitarka (2016) rupture model, and this is the only mechanism for generating asymmetry across the vertical fault in a laterally homogenous Earth model. The dipping planar fault (case 2) shown in Figure 6b shifts the axis of symmetry in the PGV toward the surface projection of the dip direction (the hanging wall). The PGV map demonstrates stronger motions on the hanging wall above the dipping fault east of the top of the rupture and weaker motions on the footwall to the west. This is due to the geometric effect of proximity of the rupture to sites on the hanging wall and larger distances on the footwall. This hanging-wall effect is seen in data from thrust events such as the 1994 Northridge earthquake (Abrahamson and Somerville, 1996) and in finite-fault simulations (e.g., Oglesby et al., 2000; Aagaard et al., 2001, 2004; Donahue and Abrahamson, 2014). The curved fault honoring the geometry specified in the USGS 3D model (case 3, Fig. 6c) shows a very similar PGV map to that of the planar fault (case 2, Fig. 6b) with stronger motions shifted above the dipping fault relative to the vertical fault. Off the southern end of the fault (X = 30–50 km), in which the planar and curved faults are nearly coincident, the PGV patterns are remarkably similar.

The PGV maps for the three fault geometries in the 3D USGS Earth model (cases 4–6) are shown in Figure 6d–f. Here, the response is more complex due to wave propagation (path and site effects) in the 3D model. PGV values are higher in the 3D model, particularly east of the HF due to low upper crustal wavespeeds of the Great Valley Sequence. This is seen for the vertical fault (case 4, Fig. 6d) especially northeast of the rupture where directivity and path effects likely contribute higher PGV values. PGV values are low on the San Leandro Gabbro despite being coincident with the fault (see Fig. 3 for the shear-wavespeed map for this domain). These patterns are also seen in the M_w 7.0 simulations shown in Figure 1. The dipping planar fault in the 3D model (case 5, Fig. 6e) shows higher PGV values on the hanging wall east of the HF and lower values on the footwall to the west relative to the vertical fault (case 4, Fig. 6d). A similar pattern is seen for the curved fault simulations using the 3D model (case 6) in Figure 6f. For both the planar and curved faults (cases 5 and 6, Figs. 6e,f), the higher PGV
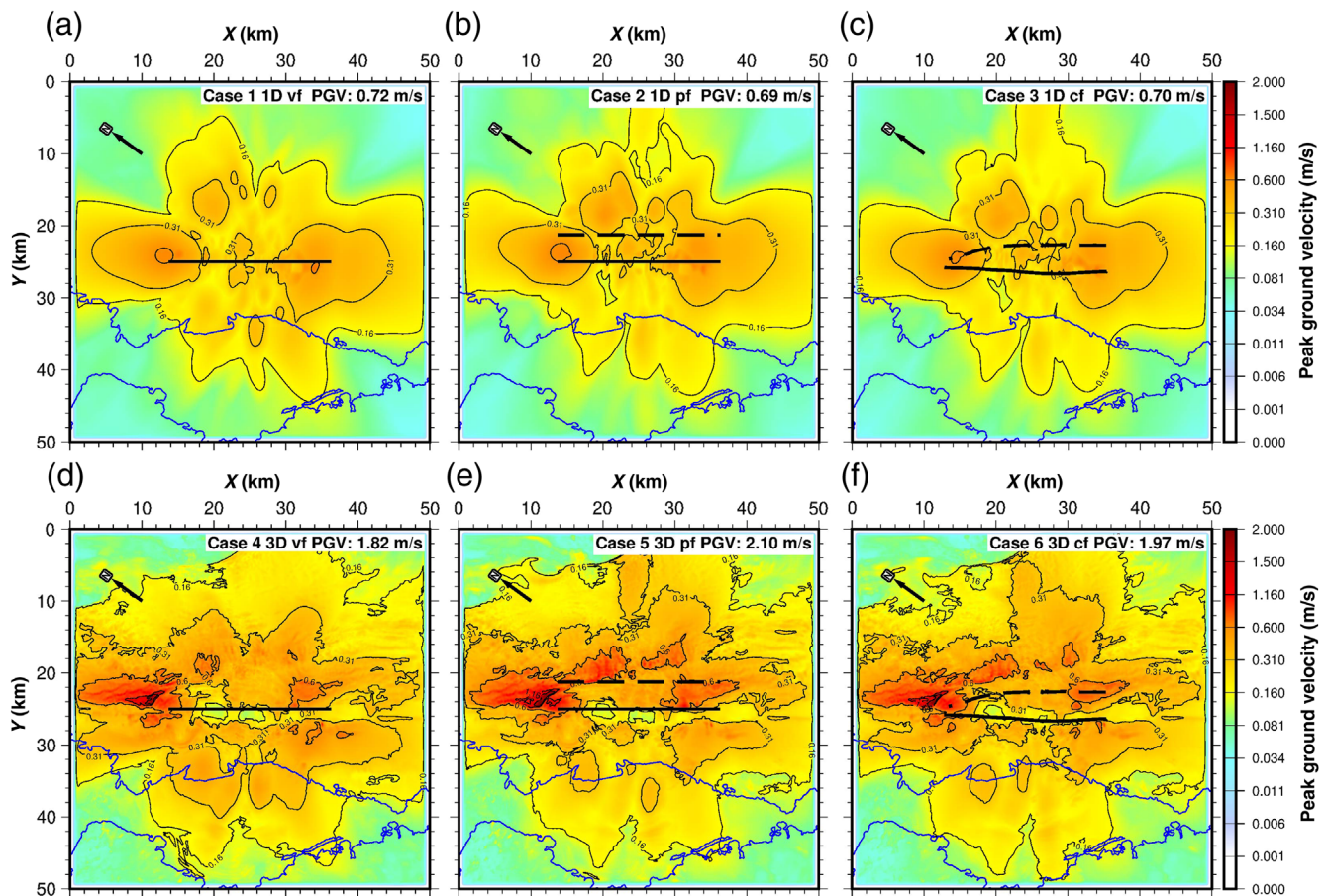
Figure 6. PGV in the 1D and 3D models for three fault geometries. (a) Case 1, 1D model, vertical fault; (b) case 2, 1D model, planar-dipping fault; (c) case 3, 1D model, curved fault; (d) case 4, 3D model, vertical fault; (e) case 5, 3D model, planar-dipping fault; (f) case 6, 3D model, curved fault. PGV is plotted according to the scale. The surface projections of the top and bottom of the fault are indicated as solid and dashed black lines, respectively. The coastline is drawn as blue lines and the orientation of the *x*- and *y* axis is shown in Figure 2. The color version of this figure is available only in the electronic edition.

values on the hanging wall extend to greater distances from the fault than for the vertical fault (case 4, Fig. 6d).

    To isolate the differences between the three fault geometries, we formed pointwise ratios of the dipping planar-to-vertical (case 2/case 1 and case 5/case 4) and curved-to-vertical (case 3/case 1 and case 6/case 4) PGV maps shown in Figure 6. To illustrate amplification and deamplification equally, we took the natural logarithm of the PGV ratio and plotted it in Figure 7 as PGV ratio maps. In these plots, the contour lines indicate linear ratios of ±25% and ±50%. To quantify differences on the hanging and footwalls, we computed mean PGV ratios for the eastern (hanging wall) and western (footwall) within the domains indicated by the gray boxes. These values are reported in each panel. We also report the minimum and maximum linear PGV ratios in each panel. For all four ratio maps, the maximum amplification or deamplification due to fault geometry is approximately a factor of 2 (linear ratios of about 0.5 and 2).

    Figure 7a shows the PGV ratio map for the 1D model planar dipping fault divided by the vertical fault PGV map (case 2/case 1), whereas Figure 7b shows the same for the

curved fault divided by the vertical fault (case 3/case 1). These PGV ratio maps show that the ground motions are stronger on the hanging wall with more than 50% amplification of PGV relative to the vertical fault within 10 km of the fault. Near the fault PGV is reduced on the footwall by less than 25%, a somewhat lesser degree than it is amplified on the hanging wall. Average linear ratios for the eastern and western sides of the fault show that intensities are increased by 7% on the hanging wall and reduced by 7% on the footwall for the 1D model planar-to-vertical PGV ratio (case 2/case 1, Fig. 7a). The 1D model curved-to-vertical PGV ratio (case 3/case 1, Fig. 7b) shows reduction in amplitudes on the footwall by 6%, but no net change on the hanging wall (eastern linear ratio = 1.00). However, strong variations with both increases and decreases in PGV are seen on the eastern side of the fault and these extend from the fault centroid normal to the fault. In particular, PGV increases by up to 50% or more on the hanging wall within 10 km of the fault trace. This effect may be most important because PGV is higher at these close distances.

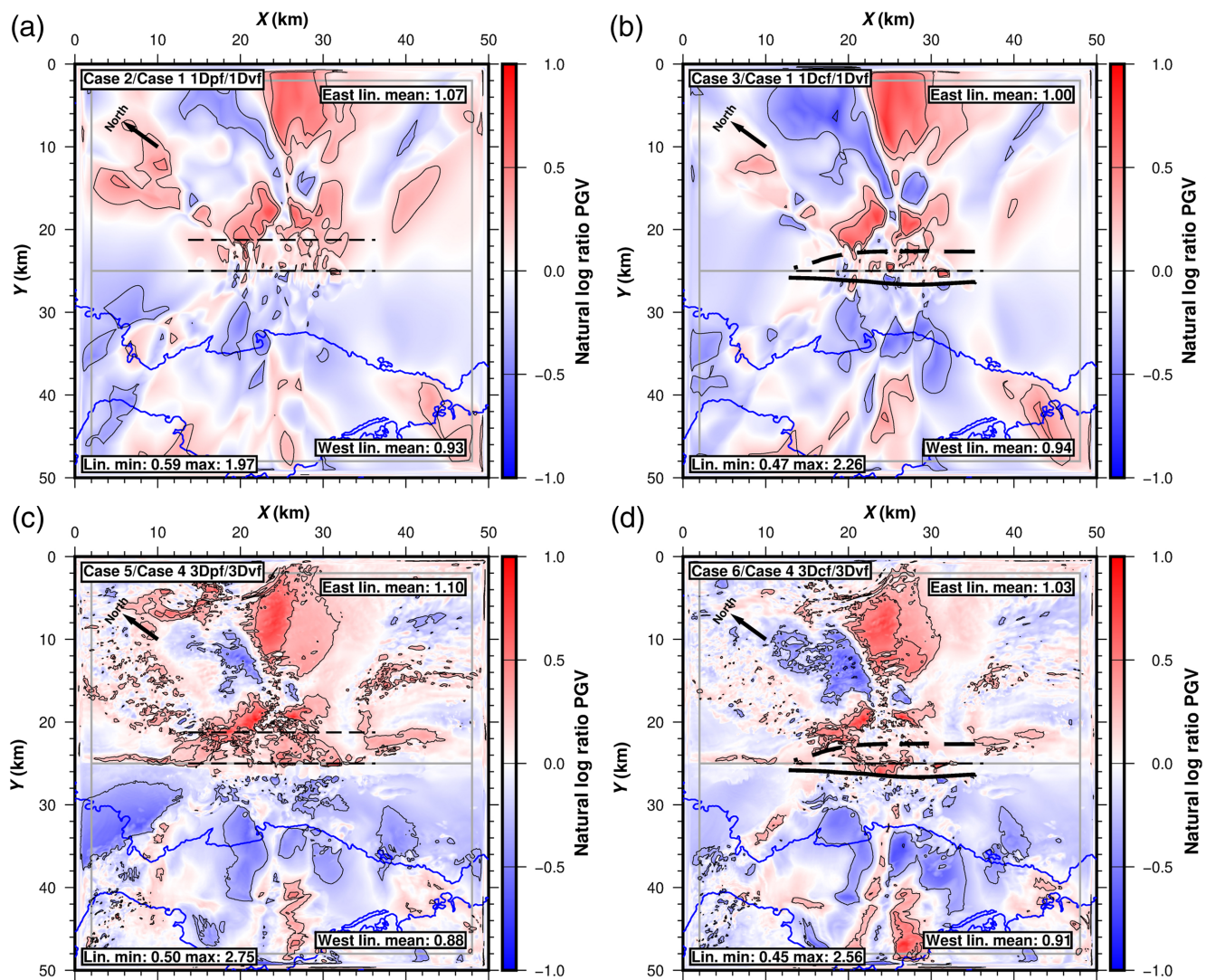   The 3D model PGV ratio maps (Fig. 7c,d) show a more complex pattern than the 1D model for the same reasons that

Figure 7. PGV ratio maps for the 1D and 3D models for three fault geometries, (a) 1D model, planar-to-vertical (case 2/case 1); (b) 1D model, curved-to-vertical (case 3/case 1); (c) 3D model, planar-to-vertical (case 5/case4); (d) 3D model, curved-to-vertical (case 6/case 4). The natural logarithm PGV ratio is plotted according to the scale. Contour lines indicate linear ratios of ±25% and ±50%. The surface projections of the top and bottom of the fault are indicated as solid and dashed black lines, respectively. The coastline is drawn similar to Figure 6. Linear PGV ratio statistics are reported on each panel, the eastern and western regions delineated by the gray boxes. The color version of this figure is available only in the electronic edition.

the constituent PGV maps are complex—path and site effects. These PGV ratio maps show clear increases of up to 50% or more in PGV on the hanging wall near the fault and to a lesser extent decreases in PGV on the footwall. In summary, the dipping geometry of the strike-slip HF results in as much as 50% stronger motions on the hanging wall (east of the HF) than would be expected from a vertical fault. On the footwall west of the HF, the motions are reduced but not to the degree they are increased on the hanging wall.

The Impact of Minimum Shear Wavespeed on Ground Motions

In this section, we describe simulations designed to investigate the effect of $V_{S\min}$ on earthquake ground motions

with the USGS 3D model. We used the curved 3D fault geometry and same domain considered in the previous sections (Fig. 2) with a smaller minimum grid spacing $h_{\min}$ of 12.5 m. In these cases, we varied the minimum shear wavespeed $V_{S\min}$ and low-pass frequency $f_{\max}$ (cases 7–9 in Table 1). These cases use the same grid spacing, surface topography, and identical mesh geometry, but only differ in $V_{S\min}$ and/or the source prefilter. Cases 7–9 used a finer minimum grid spacing of 12.5 m compared with 25 m in cases 1–6 (Table 1). Consequently, cases 7–9 had approximately eight times (8×) more grid points and required more memory and computational resources to perform.

Case 7 uses an $h_{\min}$ of 12.5 m, a $V_{S\min}$ of 250 m/s and resolves motions up to frequencies of 2.5 Hz at 8 PPW. Cases 8 and 9 use an $h_{\min}$ of 12.5 m and a $V_{S\min}$ of 500 m/s, capable
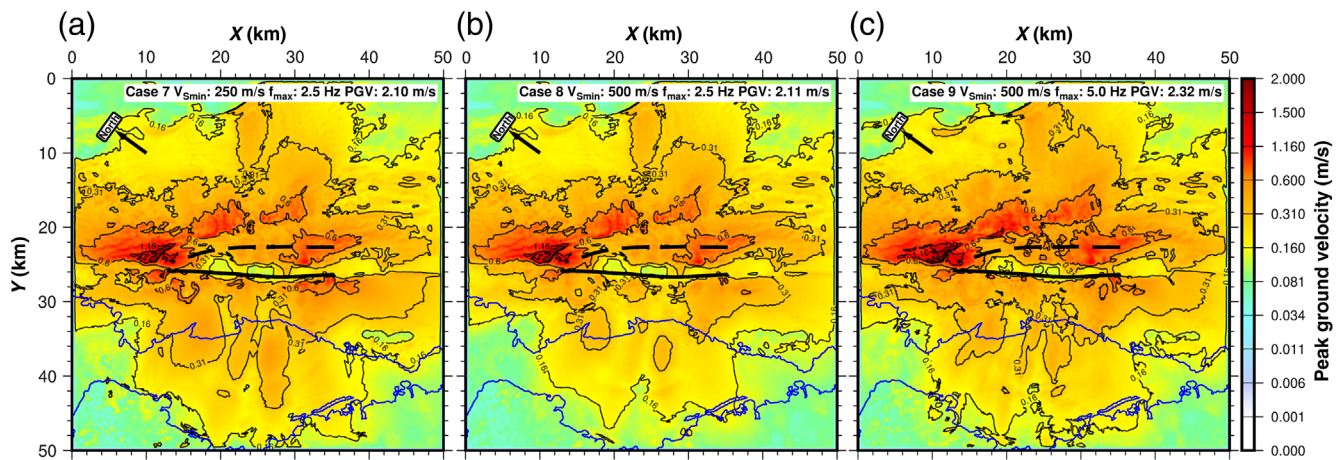
Figure 8. PGV for cases (a) 7, (b) 8, and (c) 9. PGV is plotted according to bar, similar to Figure 6. The color version of this figure is available only in the electronic edition.

of resolving motions to 5.0 Hz at 8 PPW. However, we use the SW4 source prefilter feature to low-pass filter motions to 2.5 and 5.0 Hz for cases 8 and 9, respectively. Consequently, case 9 includes resolved frequencies in the band 2.5–5.0 Hz that case 8 does not. The differences between the shear wave-speeds for case 7 with $V_{S\min} = 250$ m/s and all other cases ($V_{S\min} = 500$ m/s) can be seen from inspection of Figure 3a. Lowering $V_{S\min}$ to 250 m/s lowers the surface V_S in the Franciscan Complex west of the HF by about a factor of 2, but does not change any of the material properties in the Great Valley Sequence east of the HF. These changes only impact the near-surface (depths < 75 m) shear-wavespeed structure west of the HF.

Figure 8 shows the PGV maps for cases 7, 8, and 9 along with peak values for the domain similar to Figure 6. The overall pattern of intensities is similar to case 6 (Fig. 6f), which used the same curved fault geometry from the USGS 3D model but a $V_{S\min}$ of 500 m/s and a $h_{\min}$ of 25 m to resolve 2.5 Hz. Differences in these PGV maps are subtle but reveal the impact of the assumed $V_{S\min}$ in the simulations. Case 7 with lower $V_{S\min}$ of 250 m/s (Fig. 8a) is perhaps the most realistic case because it most closely honors the low geotechnical V_S values in the USGS 3D model. It shows the strongest motions on the west side of the HF in the urbanized East Bay and shoreline of any case considered with areas experiencing PGV in excess of 0.6 m/s. Case 8 with higher $V_{S\min}$ of 500 m/s (Fig. 8b) shows reduced PGV along the East Bay shoreline compared to case 7. Case 9 with higher $V_{S\min}$ of 500 m/s but resolving motions up to 5 Hz (Fig. 8c) shows strong PGV values (> 0.3 m/s) across most of the urbanized Easy Bay shore, similar to case 7 (Fig. 8a). All three cases show a similar pattern of PGV values in the Great Valley Sequence east of the HF, with the higher frequency response in case 9 having the highest PGV values (2.32 m/s).

To emphasize the differences in ground-motion intensity with different assumed $V_{S\min}$, we form PGV ratio maps as we did to investigate the effects of fault geometry. Figure 9 shows

the natural logarithm of the ratio of PGV maps from different cases. The impact of lowering the $V_{S\min}$ is seen in Figure 9a for case 7/case 8 showing the ratio of $V_{S\min} = 250$ and 500 m/s with motions resolved to 2.5 Hz. The lower $V_{S\min}$ value of 250 m/s (case 7) includes low wavespeed near-surface materials in the urbanized areas of Oakland, Berkeley, San Leandro, Hayward, Fremont, and East Bay shoreline. These lower V_S values result in higher motions compared to the case with $V_{S\min}$ of 500 m/s (case 8), so PGV ratio maps show amplification (red) west of the HF. On average, the motions are 25% higher across the entire western side of the HF, but close to the fault the motions can be larger by more than a factor of 3 (Fig. 9a). Not surprisingly, there are no noticeable differences on the east side of the HF because there a $V_{S\min}$ of 500 m/s captures the lowest values in the USGS 3D model.

From the PGV ratio map for case 9/case 8, we can see how the higher frequency 5 Hz motions resolved in case 9 differ from motions computed to 2.5 Hz in case 8 with constant $V_{S\min}$ of 500 m/s (Fig. 9b). Overall, this map shows that 5 Hz motions (case 9) are higher almost everywhere (on average 15% higher). Large amplifications of nearly a factor of 3 are seen close to the HF in the urbanized East Bay area. Amplifications in the East Bay Hills, east of the HF, appear to be related to topographic features.

Figure 9c shows the case 7/case 9 PGV ratio map. These calculations use an identical mesh but differ in their $V_{S\min}$ and $f_{\max}$ values (Table 1). This map shows that using a lower $V_{S\min}$ and resolving up to 2.5 Hz (case 7) results in higher PGV values in the Franciscan Complex west of the HF compared to choosing twice the $V_{S\min}$ and resolved frequency (5.0 Hz, case 9). East of the HF where the USGS 3D model specifies near-surface V_S at or above 500 m/s, the higher frequency (5 Hz) motions in case 9 result in higher PGV values (ln PGV ratios are negative, blue). This is an interesting way to consider the use of a computational resource. Both calculations use the same number of grid points, memory,
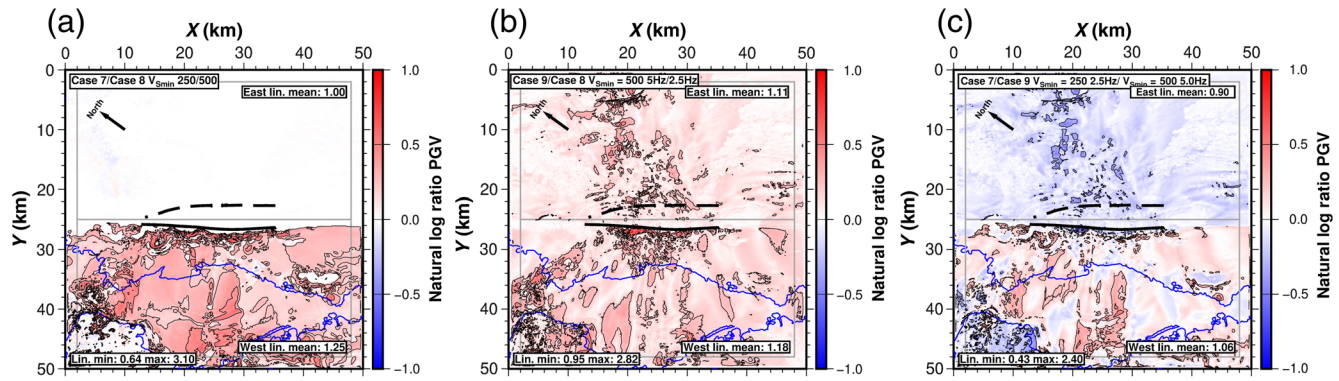
Figure 9. PGV ratio maps for (a) case 7 ($V_{S\min} = 250$ m/s)/case 8 ($V_{S\min} = 500$ m/s), (b) case 9 ($V_{S\min} = 500$ m/s, $f_{\max} = 5$ Hz)/case 8 ($V_{S\min} = 500$ m/s, $f_{\max} = 2.5$ Hz), and (c) case 7 ($V_{S\min} = 250$ m/s, $f_{\max} = 2.5$ Hz)/case 9 ($V_{S\min} = 500$ m/s, $f_{\max} = 5$ Hz) similar to Figure 7. Linear PGV ratio statistics are reported on each panel, the eastern and western regions delineated by the gray boxes. The color version of this figure is available only in the electronic edition.

and computational effort. Choosing a lower $V_{S\min}$ to more closely honor the reported geotechnical properties results in higher shaking intensity in areas with lower near-surface V_S values compared to results assuming double the $V_{S\min}$ and resolving double the frequency. These results inform us what has been missed by assuming a higher $V_{S\min}$ value of 500 m/s and resolving higher frequency motions. In particular, Figure 9a suggests that motions from recent studies (Fig. 1; Rodgers, Pitarka, *et al.*, 2018; Rodgers *et al.*, 2019) may underestimate peak shaking intensities by 25% in the densely populated areas (e.g., Hayward, Oakland, Berkeley) in Franciscan Complex geology west of the HF (and maybe more if we captured even lower wavespeed near-surface properties in the USGS 3D model).

We now consider the effect of the assumed minimum shear wavespeed on ground-motion time histories and their spectral content. Figure 10 shows PGV ratio map (case 7/case 8) with the locations of eight selected sites. This PGV ratio quantifies the effect of lowering $V_{S\min}$ from 500 to 250 m/s for the curved fault in the USGS 3D model using simulations resolved to 2.5 Hz. Site locations are named S_XX_YY, in which XX and YY are the cartesian X- and Y-coordinates in kilometers. Figure 11 shows plots of the waveforms and Fourier amplitude spectra at the eight sites selected to sample the diversity of responses. These plots show both horizontal components of velocities (X is fault parallel and Y is fault normal) on the same amplitude scale. Also shown are the Fourier amplitude spectra for each waveform with Konno–Ohmachi smoothing (Konno and Ohmachi, 1998) and the spectral ratios for case 7 ($V_{S\min} = 250$ m/s) divided by case 8 ($V_{S\min} = 500$ m/s) for each component along with the average. The waveforms show that the lower $V_{S\min}$ amplifies and delays the arrival of energy. The spectra show that energy in the velocity ground motions is predominately concentrated in the frequency band 0.2–2.0 Hz.

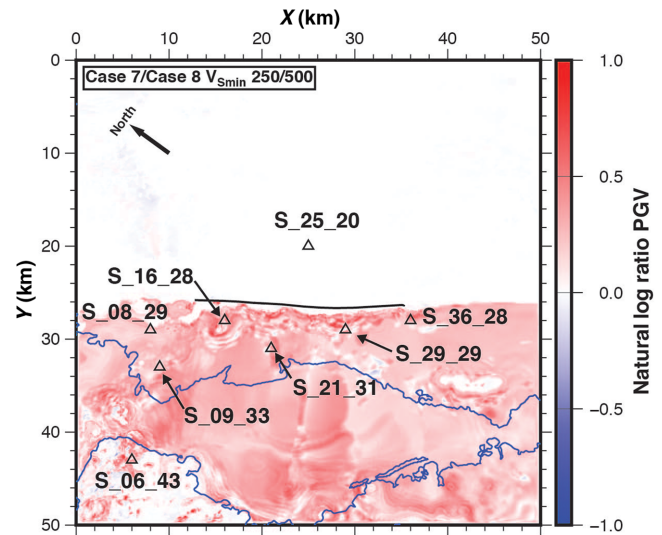No differences in the time- or frequency-domain response are seen at site S_25_20 located in the Great Valley

Figure 10. Map showing locations of sites (triangles) where seismograms and spectra are compared for cases 7 and 8 in Figure 11 along with the PGV ratio map for case 7/case 8. Sites are labeled *S_XX_YY* in which *XX* and *YY* are the *X*- and *Y*- coordinates in kilometers. The coastline and orientation are similar to Figure 3. The color version of this figure is available only in the electronic edition.

Sequence, east of the HF. For this path and site, the two Earth models for cases 7 and 8 are essentially identical and no difference is expected. However, large differences in the waveforms and spectra are seen at other sites. All sites west of the HF show amplification above 0.5 Hz. The lower $V_{S\min}$ of 250 m/s in case 7 results in higher amplitudes in the largest pulses, more reverberations, and longer duration on both the fault-normal (X) and fault-parallel (Y) components. In the frequency domain, these differences appear as higher spectral amplitudes for $V_{S\min} = 250$ m/s. Average spectral ratios are peaked between 0.5 and 1.5 Hz, with peak values between 2 and 4. Site S_29_29 (near Hayward) shows the largest spectral ratio values due to peaks in the individual
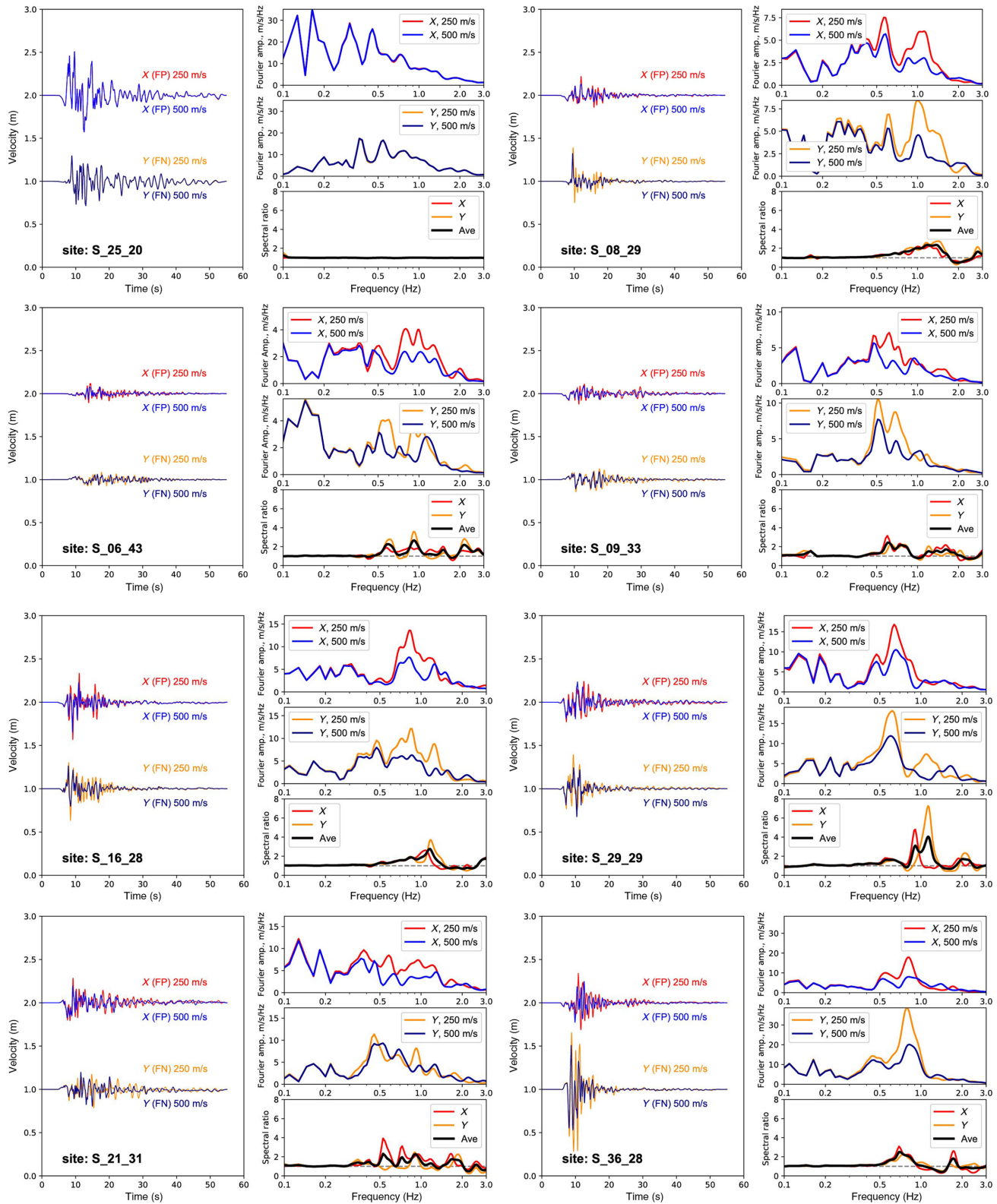
Figure 11. Horizontal-component seismograms, spectra, and spectral ratios at eight sites shown in Figure 10 for case 7 ($V_{S\,\mathrm{min}} = 250$ m/s) and case 8 ($V_{S\,\mathrm{min}} = 500$ m/s). For each site, the waveforms are shown on the left with spectra for the fault-parallel (FP, X) and fault-normal (FN, Y) components (right upper) and spectral ratios (lower right). The color version of this figure is available only in the electronic edition.

component spectral ratios. S_06_43 (San Francisco) has weaker motions due to longer distance, but spectral ratios show peaks at 0.6 and 0.9 Hz.

Let us now consider the spectral amplification at this upper end of resolved frequencies (0.5–1.5 Hz) for sites west of the HF (Fig. 11). This amplification is not surprising because the differences in the Earth models for cases 7 and 8 are limited to the geotechnical near-surface properties. Figure 4a shows the near-surface shear-wavespeed profile for a similar location in Oakland but is representative of the areas sampled by the waveforms in Figure 11. The limitation of shear wavespeed to values at or above 250 (case 7) or 500 m/s (case 8) results in changes to the upper 75 m of the profile. The resonant frequency for a vertically propagating horizontally polarized shear wave to a (1D) layer of thickness $H = 75$ m with shear wavespeed V_S between 250 and 350 m/s, $f_R = V_S/4 \times H = 0.83$–1.2 Hz. This frequency band corresponds roughly to the peaks in the spectral ratios in Figure 11. Of course, the response computed by SW4 includes the full 3D wave propagation response (with topography) for waves propagating in all directions excited by radiation from a large fault surface, so direct comparison with the simplified 1D response is a crude approximation. However, the amplification seen in the spectral ratio makes sense in terms of this simple model. Furthermore, the assumption of a lower $V_{S\min} = 250$ m/s in case 7 makes no difference in the lower frequencies, say below 0.5 Hz, compared with case 8 with higher $V_{S\min}$ of 500 m/s. This shows how lower frequency (< 0.5 Hz) waves are not likely to be impacted by shallow (< 100 m) geotechnical properties with shear wavespeeds less than 500 m/s. To resolve the impact of lower wavespeed geotechnical structure, one needs to resolve wavelengths that are on the order of one half to one quarter of the thickness of near-surface layers, requiring grid spacing of at least 10–20 m.

Discussion

This article addresses the impact of fault geometry and the assumed minimum shear wavespeed on 3D ground-motion simulations. Simulation studies of large ($M_w \sim 7.0$) HF earthquakes with the USGS 3D model of the SFBA (USGS, 2019) have shown asymmetry in the ground-motion intensity across the fault (Aagaard *et al.*, 2010; Johansen *et al.*, 2017; Rodgers, Petersson, *et al.*, 2018; Rodgers, Pitarka, *et al.*, 2018; Rodgers *et al.*, 2019). This was often attributed to lithologic heterogeneity due to different geologic units on either side of the fault. The sedimentary Great Valley Sequence east of the HF has deeper low-wavespeeds than the Franciscan Complex rocks west of the HF (Figs. 3 and 4). Previous simulation studies generally assumed a higher minimum shear wavespeed ($V_{S\min}$) than the values specified by the USGS 3D model for the SFBA (USGS, 2019) and the role of the east-dipping nature of the HF and the resulting hanging-wall effects had not been investigated. We examined the impact of fault geometry and the

assumed $V_{S\min}$ on ground-motion simulations for an M_w 6.5 HF earthquake. Pairs of simulations allowed isolation of the impact of the assumed fault geometry or $V_{S\min}$ by keeping all but one model feature constant and resolving the same maximum frequency (2.5 Hz). However, additional simulations with alternative rupture models should be performed to evaluate the robustness of results obtained here.

The east-dipping fault geometry impacts ground-motion intensities around the HF, with higher shaking intensities on the hanging wall east of the fault and lower motions on the footwall to the west (Fig. 7). Amplifications of up to 50% within 10 km of the fault are obtained on the hanging wall. These are larger than the deamplifications obtained on the footwall. This indicates that that dipping fault geometry can play a role in the asymmetry seen in recent scenario earthquake ground-motion simulations (Fig. 1). Also contributing to the asymmetry across the HF are the wave propagation path and site effects caused by the complex subsurface structure. Higher amplitudes east of the fault are caused by deep low-wavespeed material in the Great Valley Sequence sedimentary rocks. West of the fault the Franciscan geology has relatively thin, low wavespeed ($V_S < 500$ m/s) near-surface geotechnical properties (< 75 m) underlain by faster hard rock ($V_S > 1000$ m/s). Investigation of the impact of the assumed minimum shear wavespeed ($V_{S\min}$) on simulated ground motions helps us understand what is missed in simulations using a $V_{S\min}$ value of 500 m/s. Assuming a $V_{S\min}$ of 250 m/s does not affect the Earth model in the Great Valley Sequence, east of the HF, because in the USGS 3D velocity model this area has near-surface V_S of 500 m/s or higher. However, west of the HF, the USGS 3D model indicates near-surface V_S less than 250 m/s (Figs. 3 and 4). Using a $V_{S\min}$ of 250 m/s results in higher amplitude motions west of the HF. On average, the amplification west of the HF is 25%, with simulation results showing some localized amplifications of as much as a factor of 3 (Fig. 9a). Waveforms show higher amplitudes and longer duration response for the lower $V_{S\min}$ (Fig. 11). Spectral ratios at collocated sites for the two cases with $V_{S\min}$ of 250 m/s divided by 500 m/s show amplification for frequencies above 0.5–1.5 Hz with component averaged amplifications of about 2–4 with some single-component spectral ratios with peak amplifications up to a factor of 7 (Fig. 11).

Assuming a lower $V_{S\min}$ of 250 m/s only slightly reduces the asymmetry seen in previous HF ground-motion simulations such as those shown in Figure 1. The shaking intensity in the Great Valley Sequence east of the HF is still quite high and dominates the response (Fig. 8a). It is important to note that assuming a $V_{S\min}$ of 250 m/s still does not honor the lowest wavespeed near-surface geotechnical properties in the Franciscan Complex west of the HF in the populated areas of Oakland, Berkeley, San Leandro, Hayward, and Fremont. These areas have near-surface V_S values between 100–200 m/s and V_{S30} values of 100–400 m/s (Holzer, Bennett, *et al.*, 2005; Holzer, Padovani, *et al.*,

2005; Yong *et al.*, 2016). Investigations of lower near-surface wavespeed effects, including nonlinear soil response, remain for further study and will demand commensurate computational improvements and resources.

The two cases considered above indicate that 3D earth structure and the deep (up to 10 km) low wavespeeds of the Great Valley Sequence are the main cause of the asymmetry seen in previous HF ground-motion simulations. Case 4 considered a vertical fault in the 3D model and showed asymmetry across the fault with the East Bay Hills having high PGV values, particularly in the northward directivity in the hills east of Berkeley and near Orinda (Fig. 6d). This area has shown high PGV values in recent simulations with two different rupture models (Fig. 1; Rodgers, Pitarka, *et al.*, 2018; Rodgers *et al.*, 2019). This case can be compared with case 1 (Fig. 6a) for the vertical fault with the 1D model, which shows a very nearly symmetric response across the fault. For the vertical fault in the 3D model, asymmetry is caused by wave propagation (path and site effects) in the 3D Earth model and higher intensity shaking is associated with low wavespeeds of the Great Valley Sequence.

The results of this study are applicable to 3D ground-motion studies in general. Many locations of interest to seismic hazard have low wavespeed ($V_S < 500$ m/s) near-surface properties, particularly sedimentary basins (e.g., Los Angeles, Seattle, Kanto Basin/Tokyo, Mexico City). The simulation results presented here inform how assumptions of $V_{S\min}$ impact the computed ground motions. Figure 9a shows that halving $V_{S\min}$ from 500 to 250 m/s results in 25% increase in PGV across a broad region where near-surface V_S is less than 500 m/s. Figure 9b shows that doubling the resolved frequency from 2.5 to 5.0 Hz while keeping $V_{S\min}$ constant at 500 m/s increases the shaking intensity with stronger increases in which near-surface V_S is actually lower than 500 m/s. Given a computational resource, one could choose a higher $V_{S\min}$ and resolve higher frequencies (e.g., case 9, $V_{S\min} = 500$ m/s and $f_{\max} = 5.0$ Hz) or choose to lower $V_{S\min}$ and resolve lower frequencies (e.g., case 7, $V_{S\min} = 250$ m/s and $f_{\max} = 2.5$ Hz). We should not expect that increasing the frequency content will always lead to increasing PGV as source properties and path attenuation will reduce amplitudes to the range of observations. This topic remains on the vanguard of earthquake source physics and computational earthquake seismology. The ratio of these PGV maps (cases 7 and 9, Fig. 9c) shows that assuming a lower $V_{S\min}$ and lower $f_{\max}$ results in higher shaking intensities in which the near-surface wavespeeds are lower than 500 m/s. These results highlight the need to represent lower near-surface geotechnical properties and further motivate improvements of computational algorithms and the use of more powerful computational platforms to advance earthquake ground-motion simulations. Despite improvements in algorithms and access to more powerful computers, we would still need to lower the $V_{S\min}$ to more faithfully honor the USGS 3D model and resolve higher frequencies to 5–10 Hz.

One algorithmic improvement underway for SW4 is adding mesh refinement within the curvilinear grid (Wang and Petersson, unpublished manuscript, 2018; see Data and Resources). The curvilinear grid is needed to represent the nonplanar free surface for the rough topography and bathymetry of the SFBA. Topography impacts high-frequency motions of engineering interest. Allowing the grid spacing to vary in the curvilinear mesh will enable high-frequency simulations with fewer grid points and efficient use of memory.

Finally, the accuracy of the USGS 3D model needs to be thoroughly evaluated by comparing simulated waveforms with moderate (M_w 3.5–5.5) earthquake recordings. Previous work considered moderate earthquake waveforms for an earlier version of the model (Rodgers *et al.*, 2008; Aagaard *et al.*, 2010; Kim *et al.*, 2010; Rodgers, Petersson, *et al.*, 2018). These studies offered encouragement that simulated waveforms for frequencies below 1.0 Hz could reproduce observed behavior for limited events and paths. Clearly more systematic study of the 3D model is needed to evaluate the path- and region-specific performance of the current 3D model as well as identify specific changes to the model that are needed to improve fits.

Conclusions

We investigated the impact of fault geometry and the assumed $V_{S\min}$ on ground-motion intensities for an M_w 6.5 earthquake on the HF, though the results of this study are applicable to 3D ground-motion simulations in general. The east-dipping nature of the HF increases intensities on the hanging wall and also contributes to the large motions seen in the Great Valley Sequence in previous studies. Changing fault geometry from vertical to the curved fault following USGS 3D model increases motions east of the HF by up to 50% in isolated areas (Fig. 7c). Reducing $V_{S\min}$ to better honor the low near-surface wavespeeds in the Franciscan Complex west of the HF increases PGV by 25% on average with isolated locations amplified by up to a factor of 3 (Fig. 9a). This suggests that in previous studies ground motions along the populated East Bay shoreline are underestimated for frequencies above 0.5 Hz. The asymmetry in PGV across the HF for rupture in the USGS 3D model is large (up to a factor of 2) and exists regardless of fault geometry (Fig. 6d,e,f) for $V_{S\min}$ set to 500 m/s. This asymmetry in PGV seen in previous studies persists after reducing $V_{S\min}$ from 500 to 250 m/s. We conclude that the low shear wavespeeds at depth associated with Great Valley Sequence in the USGS 3D model give rise to the high intensities seen in this geologic unit by previous simulation studies.

Data and Resources

SW4 (seismic waves, fourth order) is an open-source seismic simulation code developed at Lawrence Livermore National Laboratory (LLNL) and distributed by the

Computational Infrastructure for Geodynamics (https://github.com/geodynamics/sw4). Simulations were performed using an allocation on Cori Phase-2 at National Energy Research Scientific Computing Center (NERSC), Lawrence Berkeley National Laboratory. The U.S. Geological Survey (USGS) 3D model of seismic structure for the San Francisco Bay Area (SFBA) was obtained from a website (USGS, 2019, https://earthquake.usgs.gov/data/3dgeologic/). Simulated ground-motion data were processed and plotted using Python and ObsPy (Krischer *et al.*, 2015), and the Generic Mapping Tool (Wessel *et al.*, 2013). The USGS 3D model was queried for analyses and plotting with the pySW4 python package, from Shahar Shani-Kadmiel (github.com/shaharkadmiel/pySW4). All websites were last accessed on April 2019. The unpublished manuscript by S. Wang and N. A. Petersson (2018), "Fourth order finite difference methods for the wave equation with mesh refinement interfaces", submitted to *SIAM J. Sci. Comput.* LLNL-JRNL–757334.

Acknowledgments

References

Aagaard, B. T., T. M. Brocher, D. Dolenc, D. Dreger, R. W. Graves, S. Harmsen, S. Hartzell, S. Larsen, K. McCandless, S. Nilsson, *et al.* (2008). Ground-motion modeling of the 1906 San Francisco earthquake, Part II: Ground-motion estimates for the 1906 earthquake and scenario events, *Bull. Seismol. Soc. Am.* **98,** no. 2, 1012–1046, doi: 10.1785/0120060410.

Aagaard, B. T., R. W. Graves, A. Rodgers, T. M. Brocher, R. W. Simpson, D. Dreger, N. A. Petersson, S. C. Larsen, S. Ma, and R. C. Jachens (2010). Ground-motion modeling of Hayward fault scenario earthquakes, Part II: Simulation of long-period and broadband ground motions, *Bull. Seismol. Soc. Am.* **100,** no. 6, 2945–2977, doi: 10.1785/0120090379.

Aagaard, B. T., J. F. Hall, and T. H. Heaton (2001). Characterization of near-source ground motions with earthquake simulations, *Earthq. Spectra* **17,** no. 2, 177–207.

Aagaard, B. T., J. Hall, and T. Heaton (2004). Effects of fault dip and slip rake angles on near-source ground motions: Why rupture directivity was minimal in the 1999 Chi-Chi, Taiwan, earthquake, *Bull. Seismol. Soc. Am.* **94,** no. 1, 155–170, doi: 10.1785/0120030053.

Abrahamson, N. A., and P. G. Somerville (1996). Effects of the hanging wall and footwall on ground motions recorded during the Northridge earthquake, *Bull. Seismol. Soc. Am.* **86,** no. 1B, S93–S99.

Abrahamson, N. A., W. Silva, and R. Kamai (2014). Summary of the ASK14 ground-motion relation for active crustal regions, *Earthq. Spectra* **30,** no. 3, 1025–1055, doi: 10.1193/070913EQS198M.

Bakun, W., B. Aagaard, B. Dost, W. Ellsworth, J. Hardebeck, R. Harris, C. Ji, M. Johnston, J. Langbein, J. Lienkaemper, *et al.* (2005). Implications for prediction and hazard assessment from the 2004 Parkfield earthquake, *Nature* **437,** 969–974, doi: 10.1038/nature04067.

Bonilla, L. F., R. Archuleta, and D. Lavallee (2005). Hysteretic and dilatant behavior of cohesionless soils and their effects on nonlinear site

response: Field data, observations and modeling, *Bull. Seismol. Soc. Am.* **95,** 2373–2395.

Boore, D. M. (2004). Can site response be predicted?, *J. Earthq. Eng.* **8,** Special Issue 1, 1–41.

Boore, D. M. (2010). Orientation independent, nongeometric-mean measures of seismic intensity from two horizontal components of motion, *Bull. Seismol. Soc. Am.* **100,** 1830–1835.

Boore, D. M., J. Watson-Lamprey, and N. A. Abrahamson (2006). Orientation-independent measures of ground motion, *Bull. Seismol. Soc. Am.* **96,** no. 4A, 1502–1511.

Bozorgnia, Y., N. A. Abrahamson, L. Al Atik, T. D. Ancheta, G. M. Atkinson, J. W. Baker, A. Baltay, D. M. Boore, K. W. Campbell, B. S.-J. Chiou, *et al.* (2014). NGA-West2 research project, *Earthq. Spectra* **30,** no. 3, 973–987, doi: 10.1193/072113EQS209M.

Brocher, T. M. (2005a). Compressional and shear wave velocity versus depth in the San Francisco Bay Area, California: Rules for USGS Bay Area Velocity Model 05.0.0, *U.S. Geol. Surv. Open-File Rept. 2005-1317,* 58 pp., available at http://pubs.usgs.gov/of/2005/1317/ (last accessed April 2019).

Brocher, T. M. (2005b). A regional view of urban sedimentary basins in northern California based on oil industry compressional-wave velocity and density logs, *Bull. Seismol. Soc. Am.* **95,** 2093–2114.

Brocher, T. M. (2008). Compressional and shear-wave velocity versus depth relations for common rock types in Northern California, *Bull. Seismol. Soc. Am.* **98,** 950–968.

Campbell, K. W., and Y. Bozorgnia (2014). NGA-West2 ground motion model for the average horizontal components of PGA, PGV, and 5% damped linear acceleration response spectra, *Earthq. Spectra* **30,** 1087–1115.

Chaljub, E., D. Komatitsch, J.-P. Vilotte, Y. Capdeville, B. Valette, and G. Festa (2007). Spectral element analysis in seismology, in *Advances in Wave Propagation in Heterogeneous Media,* R. S. Wu and V. Maupin (Editors), Elsevier Academic Press, New York, New York, 365–419.

Chiou, B. S.-J., and R. R. Youngs (2014). Update of the Chiou and Youngs NGA model for the average horizontal component of peak ground motion and response spectra, *Earthq. Spectra* **30,** 1117–1153.

Donahue, J. L., and N. A. Abrahamson (2014). Simulation-based hanging wall effects, *Earthq. Spectra* **30,** no. 3, 1269–1284.

Dreger, D., and B. Romanowicz (1994). Source characterization of events in the San Francisco Bay region, *U.S. Geol. Surv. Open-File Rept. 94-176,* 301–309.

Flinchum, B. A., J. N. Louie, K. D. Smith, W. H. Savran, S. K. Pullammanappallil, and A. Pancha (2014). Validating Nevada ShakeZoning predictions of Las Vegas basin response against 1992 Little Skull Mountain earthquake records, *Bull. Seismol. Soc. Am.* **104,** no. 1, 439–450, doi: 10.1785/0120130059.

Fu, H., C. He, B. Chen, Z. Yin, Z. Zhang, W. Zhang, T. Zhang, W. Xue, W. Liu, W. Yin, *et al.* (2017). 18.9Pflopss nonlinear earthquake simulation on Sunway TaihuLight: Enabling depiction of 18-Hz and 8-meter scenarios, *Proc. of the International Conference for High Performance Computing, Networking, Storage and Analysis, SC17,* Denver, Colorado, 12–17 November 2017, doi: 10.1145/3126908.3126910.

Graves, R. W. (1996). Simulating seismic wave propagation in 3D elastic media using staggered-grid finite differences, *Bull. Seismol. Soc. Am.* **86,** 1091–1106.

Graves, R., and A. Pitarka (2015). Refinements to the Graves and Pitarka (2010) broadband ground-motion simulation method, *Seismol. Res. Lett.* **86,** doi: 10.1785/0220140101.

Graves, R., and A. Pitarka (2016). Kinematic ground-motion simulations on rough faults including effects of 3D stochastic velocity perturbations, *Bull. Seismol. Soc. Am.* **106,** no. 5, 2136–2153, doi: 10.1785/0120160088.

Graves, R. W., and A. Pitarka (2010). Broadband ground-motion simulation using a hybrid approach, *Bull. Seismol. Soc. Am.* **100,** 2095–2123, doi: 10.1785/0120100057.

Graymer, R. W., D. A. Ponce, R. C. Jachens, R. W. Simpson, G. A. Phelps, and C. M. Wentworth (2005). Three-dimensional geologic map of the Hayward fault, northern California: Correlation of rock units with variations in seismicity, creep rate, and fault dip, *Geology* **33,** no. 6, 521–524, doi: 10.1130/G21435.1.

Hardebeck, J. L., A. J. Michael, and T. M. Brocher (2007). Seismic velocity structure and seismotectonics of the eastern San Francisco Bay region, California, *Bull. Seismol. Soc. Am.* **97,** no. 3, 826–842, doi: 10.1785/0120060032.

Harmsen, S., S. Hartzell, and P. Liu (2008). Simulated ground motion in Santa Clara Valley, California, and vicinity from M ≥ 6 : 7 scenario earthquakes, *Bull. Seismol. Soc. Am.* **98,** no. 3, 1243–1271, doi: 10.1785/0120060230.

Hartzell, S. H., L. F. Bonilla, and R. A. Williams (2004). Prediction of nonlinear soil effects, *Bull. Seismol. Soc. Am.* **94,** 1609–1629.

Holzer, T. L., M. J. Bennett, T. E. Noce, and J. C. Tinsley III (2005). Shear-wave velocity of surficial geologic sediments in northern California: Statistical distributions and depth dependence, *Earthq. Spectra* **21,** no. 1, 161–177, doi: 10.1193/1.1895726.

Holzer, T. L., A. Padovani, M. J. Bennett, T. E. Noce, and J. C. Tinsley (2005). Mapping NEHRP VS30 site classes, *Earthq. Spectra* **21,** no. 2, 1–18, doi: 10.1193/1.1852561.

Johansen, H., A. Rodgers, N. A. Petersson, D. McCallen, B. Sjogreen, and M. Miah (2017). Toward exascale earthquake ground motion simulations for near-fault engineering analysis, *Comput. Sci. Eng.* **19,** 27–37, doi: 10.1109/MCSE.2017.3421558.

Joyner, W. B., and D. M. Boore (1988). Measurement, characterization, and prediction of strong ground motion, in *Recent Advances in Ground-Motion Evaluation*, J. L. Von Thun (Editor), American Society of Civil Engineers, New York, New York, 43–102.

Kamai, R., N. Abrahamson, and R. Graves (2014). Adding fling effects to processed ground-motion time histories, *Bull. Seismol. Soc. Am.* **104,** no. 4, doi: 10.1785/0120130272.

Kim, A., D. S. Dreger, and S. Larsen (2010). Moderate earthquake ground-motion validation in the San Francisco Bay Area, *Bull. Seismol. Soc. Am.* **100,** 819–825.

Komatitsch, D., and J. Tromp (1999). Introduction to the spectral element method for three-dimensional seismic wave propagation, *Geophys. J. Int.* **139,** 806–822, doi: 10.1046/j.1365-246x.1999.00967.x.

Konno, K., and T. Ohmachi (1998). Ground-motion characteristics estimated from spectral ratio between horizontal and vertical components of microtremor, *Bull. Seismol. Soc. Am.* **88,** no. 1, 228–241.

Kramer, S. (1996). *Geotechnical Earthquake Engineering*, Prentice Hall, Inc., Upper Saddle River, New Jersey, 653 pp.

Krischer, L., T. Megies, R. Barsch, M. Beyreuther, T. Lecocq, C. Caudron, and J. Wassermann (2015). ObsPy: A bridge for seismology into the scientific Python ecosystem, *Comput. Sci. Disc.* **8,** no. 1, 14,003–14,020, doi: 10.1088/1749-4699/8/1/014003.

Liu, P., R. J. Archuleta, and S. H. Hartzell (2006). Prediction of broadband ground-motion time histories: Hybrid low/high-frequency method with correlated random source parameters, *Bull. Seismol. Soc. Am.* **96,** no. 6, 2118–2130, doi: 10.1785/0120060036.

Mai, M., and G. Beroza (2002). A spatial random field model to characterize complexity in earthquake slip, *J. Geophys. Res.* **107,** no. B11, doi: 10.1029/2001JB000588.

Moczo, P., J. Kristek, and M. Galis (2014). *The Finite-Difference Modelling of Earthquake Motions: Waves and Ruptures*, Cambridge University Press, Cambridge, United Kingdom, doi: 10.1017/CBO9781139236911.

Oglesby, D. D., R. J. Archuleta, and S. B. Nielsen (2000). The three-dimensional dynamics of dipping faults, *Bull. Seismol. Soc. Am.* **90,** no. 3, 616–628, doi: 10.1785/0119990113.

Olsen, K. B., R. J. Archuleta, and J. R. Matarese (1995). Magnitude 7.75 earthquake on the San Andreas fault: Three-dimensional ground motion in Los Angeles, *Science* **270,** 1628–1632.

Pancha, A., S. K. Pullammanappallil, L. T. West, J. N. Louie, and W. K. Hellmer (2017). Large-scale earthquake-Hazard class mapping by parcel in Las Vegas Valley, Nevada, *Bull. Seismol. Soc. Am.* **107,** no. 2, 741–749, doi: 10.1785/0120160300.

Passone, L., and P. M. Mai (2017). Kinematic earthquake ground-motion simulations on Listric normal faults, *Bull. Seismol. Soc. Am.* **107,** 2980–2993, doi: 10.1785/0120170111.

Peter, D., D. Komatitsch, Y. Luo, R. Martin, N. Le Go, E. Casarotti, P. Le Loher, F. Magnoni, Q. Liu, C. Blitz, *et al.* (2011). Forward and adjoint simulations of seismic wave propagation on fully unstructured hexahedral meshes, *Geophys. J. Int.* **186,** no. 2, 721–739.

Petersson, N. A., and B. Sjogreen (2012). Stable and efficient modeling of anelastic attenuation in seismic wave propagation, *Comm. Comput. Phys.* **12,** no. 1, 193–225, doi: 10.4208/cicp.201010.090611a.

Petersson, N. A., and B. Sjogreen (2014). Super-grid modeling of the elastic wave equation in semi-bounded domains, *Comm. Comput. Phys.* **16,** 913–955.

Petersson, N. A., and B. Sjogreen (2015). Wave propagation in anisotropic elastic materials and curvilinear coordinates using a summation-by-parts finite difference method, *J. Comp. Phys.* **299,** 820–841, doi: 10.1016/j.jcp.2015.07.023.

Petersson, N. A., and B. E. Sjogreen (2018). *SW4 Users Guide*, Version 2.0, Lawrence Livermore National Laboratory, LLNL-SM–741439, available at https://geodynamics.org/cig/software/sw4 (last accessed April 2019).

Pitarka, A. (1999). 3D elastic finite-difference modelling of seismic motion using staggered-grid with non-uniform spacing, *Bull. Seismol. Soc. Am.* **89,** 54–68.

Pitarka, A., H. K. Thio, P. Somerville, and L. F. Bonilla (2013). Broadband ground-motion simulation of an intraslab earthquake and nonlinear site response: 2010 Ferndale, California, earthquake case study, *Seismol. Res. Lett.* **84,** no. 5, 785–795, doi: 10.1785/0220130031.

Ponce, D. A., T. G. Hildenbrand, and R. C. Jachens (2003). Gravity and magnetic expression of the San Leandro Gabbro with implications for the geometry and evolution of the Hayward fault zone, northern California, *Bull. Seismol. Soc. Am.* **93,** no. 1, 14–26.

Ponce, D. A., R. W. Simpson, R. W. Graymer, and R. C. Jachens (2004). Gravity, magnetic, and high-precision relocated seismicity profiles suggest a connection between the Hayward and Calaveras faults, northern California, *Geochem. Geophys. Geosyst.* **5,** no. 7, Q07004, doi: 10.1029/2003GC000684.

Rodgers, A., N. A. Petersson, S. Nilsson, B. Sjogreen, and K. McCandless (2008). Broadband waveform modeling of moderate earthquakes in the San Francisco Bay Area and preliminary assessment of the USGS 3D seismic velocity model, *Bull. Seismol. Soc. Am.* **98,** 969–988, doi: 10.1785/0120060407.

Rodgers, A., N. A. Petersson, A. Pitarka, and D. McCallen (2018). Simulation of large scenario and recorded moderate earthquakes in the San Francisco Bay Area, *Proc. of the 11th National Conference on Earthquake Engineering, Earthquake Engineering Research Institute*, Los Angeles, California, 25–29 June 2018, Paper ID 366.

Rodgers, A., N. A. Petersson, A. Pitarka, D. McCallen, B. Sjogreen, and N. Abrahamson (2019). Broadband (0-5 Hz) fully deterministic 3D ground motion simulations of a magnitude 7.0 Hayward fault earthquake: comparison with empirical ground motion models and 3D path and site effects from source normalized intensities, *Seismol. Res. Lett.* doi: 10.1785/0220180261.

Rodgers, A., A. Pitarka, N. A. Petersson, B. Sjogreen, and D. McCallen (2018). Broadband (0-4 Hz) ground motions for a magnitude 7.0 Hayward fault earthquake with 3D structure and topography, *Geophys. Res. Lett.* **45,** doi: 10.1002/2017GL076505.

Roten, D., K. B. Olsen, and S. M. Day (2017). Off-fault deformations and shallow slip deficit from dynamic rupture simulations with fault zone plasticity, *Geophys. Res. Lett.* **44,** no. 15, 7733–7742.

Roten, D., K. B. Olsen, S. M. Day, Y. Cui, and D. Fäh (2014). Expected seismic shaking in Los Angeles reduced by San Andreas fault zone plasticity, *Geophys. Res. Lett.* **41,** 2769–2777, doi: 10.1002/2014GL059411.

Shi, J., and D. Asimaki (2018). A generic velocity profile for basin sediments in California conditioned on V_{S30}, *Seismol. Res. Lett.* **89,** no. 4, 1397–1409, doi: 10.1785/0220170268.

Sjogreen, B., and N. A. Petersson (2012). A fourth order accurate finite difference method for the elastic wave equation in second order formulation, *J. Sci. Comput.* **52,** no. 1, 17–48, doi: 10.1007/s10915-011-9531-1.

Sneed, M., P. V. P. Orlando, J. W. Borchers, R. Everett, M. Solt, M. McGann, H. Lowers, and S. Mahan (2015). Lithostratigraphic, borehole-geophysical, hydrogeologic, and hydrochemical data from the East Bay Plain, Alameda County, California, *U.S. Geol. Surv. Data Series 890*, 56 pp., doi: 10.3133/ds890.

Somerville, P., K. Irikura, R. Graves, S. Sawada, D. Wald, N. Abrahamson, Y. Iwasaki, T. Kagawa, N. Smith, and A. Kowada (1999). Characterizing crustal earthquake slip models for the prediction of strong ground motion, *Seismol. Res. Lett.* **70**, 199–222.

Taborda, R., and J. Bielak (2011). Large-scale earthquake simulation: Computational seismology and complex engineering systems, *Comput. Sci. Eng.* **13**, 14–27, doi: 10.1109/MCSE.2011.19.

Taborda, R., S. Azizzadeh-Roodpish, N. Khoshnevis, and K. Cheng (2016). Evaluation of the southern California seismic velocity models through simulation of recorded events, *Geophys. J. Int.* **205**, no. 3, 1342–1364, doi: 10.1093/gji/ggw085.

U.S.Geological Survey (USGS) (2019). *3-D Geologic and Seismic Velocity Models of the San Francisco Bay Region*, available at https://earthquake.usgs.gov/data/3dgeologic (last accessed March 2019).

Waldhauser, F., and W. L. Ellsworth (2002). Fault structure and mechanics of the Hayward fault, California, from double-difference earthquake locations, *J. Geophys. Res.* **107**, no. B3, doi: 10.1029/2000JB000084.

Waldhauser, F., and D. P. Schaff (2008). Large-scale relocation of two decades of Northern California seismicity using cross-correlation and double-difference methods, *J. Geophys. Res.* **113**, no. B08311, doi: 10.1029/2007JB005479.

Wessel, P., W. H. F. Smith, R. Scharroo, J. F. Luis, and F. Wobbe (2013). Generic Mapping Tools: Improved version released, *Eos Trans. AGU* **94**, 409–410.

Wills, C. J., and K. B. Clahan (2006). Developing a map of geologically defined site-condition categories for California, *Bull. Seismol. Soc. Am.* **96**, no. 4, 1483–1501.

Yong, A., E. M. Thompson, D. Wald, K. L. Knudsen, J. K. Odum, W. J. Stephenson, and S. Haefner (2016). Compilation of V_{S30} data for the United States, *U.S. Geol. Surv. Data Series 978*, 8 pp., doi: 10.3133/ds978.

Arthur J. Rodgers
Arben Pitarka
Atmospheric, Earth and Energy Division and Geophysical Monitoring Program
Lawrence Livermore National Laboratory
7000 East Avenue, L-046
Livermore, California 94551 U.S.A.
rodgers7@llnl.gov

David B. McCallen
Earth and Environmental Sciences Area
Lawrence Berkeley National Laboratory
1 Cyclotron Road, MS74R316C
Berkeley, California 94720 U.S.A.